Onset of Flow Recirculation in Vertical Rotating-Disc Chemical Vapor Deposition Reactors

Joungmo Cho and T. J. Mountziaris
Dept. of Chemical Engineering, University of Massachusetts, Amherst, MA 01003

DOI 10.1002/aic.14179
Published online July 30, 2013 in Wiley Online Library (wileyonlinelibrary.com)

Preventing flow recirculation during the epitaxial deposition of thin films of compound semiconductors is essential for growing multilayer films with atomically abrupt interfaces that form a basis for modern optoelectronic devices. A mathematical model describing mass continuity, flow and heat transfer in a vertical rotating-disc chemical vapor deposition reactor is used to investigate the onset of buoyancy- and inertia-driven flow recirculation. Numerical simulations of axisymmetric flow patterns are performed and different regimes of operation are identified in the parameter space defined by the Reynolds number, the rotational Reynolds number, and the Grashof number. Design criteria for establishing recirculation-free flows in reactors used for metalorganic vapor-phase epitaxy (MOVPE) of compound semiconductors are presented. © 2013 American Institute of Chemical Engineers *AIChE J*, 59: 3530-3538, 2013
Keywords: semiconductors, reactor analysis, flow recirculation onset, metalorganic vapor phase epitaxy, design criteria

Introduction

The development of fundamental models of complex chemical engineering systems has its roots in the pioneering research of Professor Neal R. Amundson whose vision has raised awareness for the importance of mathematical models in chemical engineering.[1] The work presented in this article follows this general direction and employs mathematical modeling and computer simulations of a chemical vapor deposition reactor to elucidate complex flow phenomena that affect the quality of the deposited films, leading to design guidelines.

Vertical rotating-disc chemical vapor deposition reactors are used in the microelectronics industry for growing single crystalline films of compound semiconductors by metalorganic vapor-phase epitaxy (MOVPE).[2,3] MOVPE involves flow of a carrier gas containing vapors of organometallic film precursors over a heated susceptor. Thermal decomposition of the precursors takes place in the gas phase adjacent to the susceptor and on the surface of single-crystalline substrates placed on the susceptor resulting in epitaxial deposition of a thin film. Optimal operation of a MOVPE reactor is relevant to deposition of single-crystalline films with uniform thickness and composition, maximum utilization of expensive organometallic precursors and growth of multilayer structures with atomically-abrupt interfaces.

Complex flow patterns may arise in chemical vapor deposition reactors due to buoyancy- and inertia-driven recirculation.[4,5] Buoyancy-driven recirculation arises in a vertical rotating-disc MOVPE reactor due to flow of gas over a heated susceptor. Inertia-driven recirculation arises due to abrupt changes in the direction of flow induced by sharp geometric features or rapid susceptor rotation. Flow instabilities and breaking of symmetry in axisymmetric vertical rotating-disc MOVPE reactors have been observed experimentally and predicted by mathematical models.[4,6]

Flow recirculation can adversely affect the uniformity of films deposited by MOVPE. Trapping of precursors in recirculation regions and subsequent slow purging by diffusion during precursor switching prevent the growth of multilayer structures with abrupt interfaces. In certain cases, particles may form during MOVPE[7,8] and trapping of those particles in recirculating regions of the flow may contaminate the film, when their size exceeds a critical value that is necessary to overcome adverse thermophoretic forces and the sweeping action of the flowing gas.[9] It is common practice to operate MOVPE reactors at high-inlet flow rates and/or low pressures to prevent the formation of flow recirculation. However, this leads to short residence times and low conversions of the expensive organometallic precursors. It also increases the cost of scrubbing unused reactants from the effluent gases.

Fundamental models of flow, heat and mass transfer in MOVPE reactors have been coupled with models describing the gas-phase and surface kinetics during film growth and used to predict the film deposition rate and uniformity.[10–13] Advances in numerical techniques have enabled the use of computer simulation for design and optimization of commercial MOVPE reactors.[14–16]

The onset of flow recirculation in MOVPE reactors has been of interest as a limiting condition for reactor optimization studies aiming at identifying operating conditions that maximize film uniformity and enable the growth of multilayer structures with abrupt interfaces.[17,18] Experimental observations of flow patterns in vertical rotating-disc MOVPE reactors were combined with scaling analysis to identify analytical relationships between dimensionless numbers describing the onset of flow recirculation.[15,17] An empirical flow regime map

Correspondence concerning this article should be addressed to tjm@ecs.umass.edu.

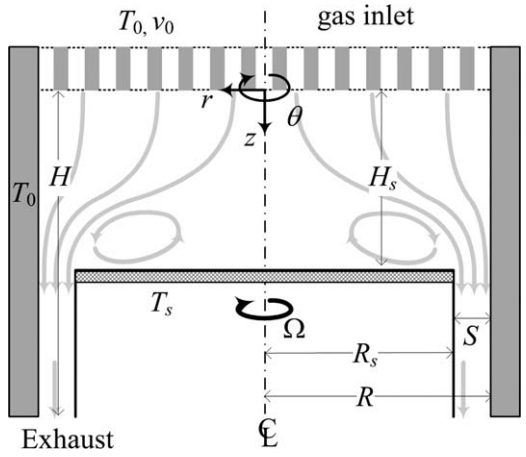

Figure 1. Schematic of a vertical rotating-disc chemical vapor deposition reactor.

was also sketched on the parameter plane defined by the susceptor temperature and rotational rate.[17]

In this work, we employ fundamental models of flow and heat transfer in a vertical rotating-disc MOVPE reactor to predict axisymmetric flow patterns and construct detailed flow regime maps in the parameter space defined by the Reynolds number, the rotational Reynolds number, and the Grashof number. The onset of flow recirculation is used to develop criteria for recirculation-free flow, guiding the reactor design and the selection of operating conditions (carrier gas flow rate, operating pressure, susceptor rotational rate), as well as geometric parameters, such as the distance of the susceptor from the reactor inlet.

Mathematical Model

The geometry of the reactor modeled in this study is shown in Figure 1. The showerhead inlet may include multiple delivery ports which introduce precursors separately, when parasitic prereactions are possible.[12,14] For the purpose of this study, it is assumed that the gas entering the reactor has a uniform downward velocity v_0. The temperature of the reactor inlet gas and side walls are set to $T_0 = 300$ K. Since in many reactors the film precursors are highly diluted in a carrier gas, such as H_2, He, Ar, or N_2, simulations of the flow and heat transfer for the carrier gas alone can predict reasonably well the flow structure in the reactor. The gas flows over a heated susceptor that is kept at a uniform temperature T_s, determined by the type of material being grown. This value can range from 600 K for some II-VI materials, such as ZnSe, to 1,500 K for III-V nitrides, such as GaN.[3] The susceptor with radius R_s is aligned with the axis of the cylindrical reactor at a distance H_s from its inlet and rotates with rotational speed, Ω. The gas flows out of the reactor through a gap formed between the susceptor and the reactor wall. The length of the channel formed between the susceptor and the reactor wall was set to be sufficiently long so that the assumption of fully developed flow at the exit of the reactor would not distort the predicted flow profile above and around the edge of the susceptor.

The flow and heat transfer in the reactor are modeled for the carrier gas alone on the assumption that the reactants are dilute enough to not affect significantly the thermophysical properties of the carrier gas. Axial symmetry and steady state are also assumed. The fundamental equations of continuity, momentum transfer, and heat transfer are written in cylindrical polar coordinates for laminar flow of an ideal gas behaving as a Newtonian fluid with physical properties that depend on temperature and pressure. Viscous dissipation is assumed to be negligible in the energy balance.

The governing equations are written in dimensionless form by defining a dimensionless radial coordinate $\hat{r}=r/R_s$, using the susceptor radius R_s for scaling the radial distances and a dimensionless axial coordinate $\hat{z}=z/H_s$, using the inlet to susceptor separation H_s, for scaling the axial distances from the reactor inlet. The axial velocity u, and radial velocity v, is scaled by the average inlet axial velocity v_0. The angular velocity, w, is scaled by the angular velocity of the edge of disc $R_s\Omega$. The gas temperature is scaled by the inlet temperature T_0, which was set at 300 K. The gas pressure p, is scaled with the atmospheric pressure $p_0 = 1$ atm. The density ρ, is computed using the ideal gas law and was scaled with the density of the compressible gas at standard conditions (T_0 and p_0). The viscosity μ, thermal conductivity k, and specific heat C_p, are assumed to be independent of pressure and scaled with the corresponding values at T_0. Hydrogen, nitrogen, helium and argon are considered as carrier gases. The temperature dependence of μ, C_p and k for each gas was obtained by fitting experimental data[19] over the temperature range of 300–1,500 K (Table 1). The caret symbol '^' is used to indicate dimensionless quantities in the equations of the model.

The dimensionless modeling equations are:

Continuity equation

$$\frac{1}{\hat{r}}\frac{\partial(\hat{\rho}\hat{r}\hat{v})}{\partial\hat{r}}+\frac{1}{\alpha}\frac{\partial(\hat{\rho}\hat{u})}{\partial\hat{z}}=0 \tag{1}$$

Radial (r) component of the equation of motion

$$\hat{\rho}\left[\hat{v}\frac{\partial\hat{v}}{\partial\hat{r}}+\frac{\hat{u}}{\alpha}\frac{\partial\hat{v}}{\partial\hat{z}}-\left(\frac{\mathrm{Re}_\omega}{2\mathrm{Re}}\right)^2\frac{\hat{w}^2}{\hat{r}}\right]+\mathrm{Eu}\,\frac{\partial\hat{p}}{\partial\hat{r}}$$
$$=\frac{2}{\mathrm{Re}}\left\{\frac{1}{\hat{r}}\frac{\partial}{\partial\hat{r}}\hat{\mu}\hat{r}\left[\frac{4}{3}\frac{\partial\hat{v}}{\partial\hat{r}}-\frac{2}{3}\left(\frac{\hat{v}}{\hat{r}}+\frac{1}{\alpha}\frac{\partial\hat{u}}{\partial\hat{z}}\right)\right]\right. \tag{2}$$
$$\left.+\frac{1}{\alpha}\frac{\partial}{\partial\hat{z}}\hat{\mu}\left(\frac{\partial\hat{u}}{\partial\hat{r}}+\frac{1}{\alpha}\frac{\partial\hat{v}}{\partial\hat{z}}\right)-\frac{\hat{\mu}}{\hat{r}}\left[\frac{4}{3}\frac{\hat{v}}{\hat{r}}-\frac{2}{3}\left(\frac{\partial\hat{v}}{\partial\hat{r}}+\frac{1}{\alpha}\frac{\partial\hat{u}}{\partial\hat{z}}\right)\right]\right\}$$

Axial (z) component of the equation of motion after invoking the Boussinesq approximation

$$\hat{\rho}\left(\hat{v}\frac{\partial\hat{u}}{\partial\hat{r}}+\frac{\hat{u}}{\alpha}\frac{\partial\hat{u}}{\partial\hat{z}}\right)+\frac{\mathrm{Eu}}{\alpha}\frac{\partial\hat{p}}{\partial\hat{z}}$$
$$=\frac{2}{\mathrm{Re}}\left\{\frac{1}{\hat{r}}\frac{\partial}{\partial\hat{r}}\hat{\mu}\hat{r}\left(\frac{\partial\hat{u}}{\partial\hat{r}}+\frac{1}{\alpha}\frac{\partial\hat{v}}{\partial\hat{z}}\right)+\frac{1}{\alpha}\frac{\partial}{\partial\hat{z}}\hat{\mu}\left[\frac{4}{3\alpha}\frac{\partial\hat{u}}{\partial\hat{z}}-\frac{2}{3}\left(\frac{\partial\hat{v}}{\partial\hat{r}}+\frac{\hat{v}}{\hat{r}}\right)\right]\right\}$$
$$-\frac{4\hat{\rho}\mathrm{Gr}\left(\hat{T}-\hat{T}_{\mathrm{avg}}\right)}{\alpha^3\mathrm{Re}^2} \tag{3}$$

Table 1. Thermophysical Properties of Typical Carrier Gases

Gas	l	m	n
H_2	0.65	0.77	−0.71
He	0.67	0.71	−0.68
N_2	0.63	0.76	−0.67
Ar	0.63	0.73	−0.76

Viscosity: $\mu=\mu_0\left(\frac{T}{T_0}\right)^m$. Thermal conductivity: $k=k_0\left(\frac{T}{T_0}\right)^l$.
Specific heat: $C_p=C_{p0}\left(\frac{k}{k_0}\right)\left(\frac{T}{T_0}\right)^n$, where μ_0, k_0, and C_{p0} are the values at $T_0 = 300$K.

where $\hat{T}_{avg} = T_{avg}/T_0$ with $T_{avg} = (T_s + T_0)/2$

Azimuthal (θ) component of the equation of motion

$$\hat{\rho}\left(\hat{v}\frac{\partial \hat{w}}{\partial \hat{r}} + \frac{\hat{u}}{\alpha}\frac{\partial \hat{w}}{\partial \hat{z}} + \frac{\hat{v}\hat{w}}{\hat{r}}\right) = \frac{2}{\mathrm{Re}}\left\{\frac{1}{\hat{r}^2}\frac{\partial}{\partial \hat{r}}\left[\hat{\mu}\hat{r}^2\left(\frac{\partial \hat{w}}{\partial \hat{r}} - \frac{\hat{w}}{\hat{r}}\right)\right] + \frac{1}{\alpha^2}\frac{\partial}{\partial \hat{z}}\left(\hat{\mu}\frac{\partial \hat{w}}{\partial \hat{z}}\right)\right\} \quad (4)$$

Energy balance:

$$\hat{\rho}\hat{C}_p\left(\hat{v}\frac{\partial \hat{T}}{\partial \hat{r}} + \frac{\hat{u}}{\alpha}\frac{\partial \hat{T}}{\partial \hat{z}}\right) = \frac{2}{\mathrm{Pe}}\left[\frac{1}{\hat{r}}\frac{\partial}{\partial \hat{r}}\left(\hat{k}\hat{r}\frac{\partial \hat{T}}{\partial \hat{r}}\right) + \frac{1}{\alpha^2}\frac{\partial}{\partial \hat{z}}\left(\hat{k}\frac{\partial \hat{T}}{\partial \hat{z}}\right)\right] \quad (5)$$

The dimensionless numbers are:

The aspect ratio

$$\alpha = H_s/R_s \quad (6)$$

Reynolds number

$$\mathrm{Re} = \frac{2R_s\rho_0 v_0}{\mu_0} \quad (7)$$

rotational Reynolds number

$$\mathrm{Re}_{\omega} = \frac{4R_s^2\Omega\rho_0}{\mu_0} \quad (8)$$

Euler number

$$\mathrm{Eu} = \frac{p_0}{\rho_0 v_0^2} \quad (9)$$

Péclet number

$$\mathrm{Pe} = \mathrm{Pr}\cdot\mathrm{Re} \quad (10)$$

where $\mathrm{Pr} = \frac{C_{p0}\mu_0}{k_0}$ is the Prandtl number, and the Grashof number:

$$\mathrm{Gr} = g_z H_s^3 \beta_T (T_s - T_0)\left(\frac{\rho_0}{\mu_0}\right)^2 \quad (11)$$

where g_z is the gravitational acceleration, and β_T is a thermal expansion coefficient set to $1/T_{avg}$.

The most important dimensionless numbers are the aspect ratio, the two Reynolds numbers, and the Grashof number. The Péclet number for gas flows is proportional to the Reynolds number because the Prandtl number is approximately constant for typical carrier gases and equal to 0.7. The pressure gradients in the reactor are typically very small, making the term containing the Euler number insignificant. The ratio ($\mathrm{Gr}/\mathrm{Re}^2$) appearing in a buoyancy term in Eq. 3 is a characteristic dimensionless quantity indicating the degree of mixed convection. For low-Re flows, inertial effects are less significant and Gr/Re is the dominant dimensionless quantity. For high-Re flows, viscous effects are less significant and ($\mathrm{Gr}/\mathrm{Re}^2$) is the dominant dimensionless quantity.

The governing Eqs. 1–5 were solved numerically subject to the no-slip condition on solid surfaces. Additional boundary conditions are:

Inlet ($\hat{z}=0$ and $0 < \hat{r} < \hat{R}$): Unidirectional flow in the downward direction with uniform velocity

$$\hat{u}=1, \hat{v}=0, \hat{w}=0 \text{ and uniform temperature } \hat{T}=1. \quad (12)$$

Exit ($\hat{z}=\hat{H}$ and $1 < \hat{r} < \hat{R}$): Fully developed flow in the axial direction

$$\left(\frac{\partial \hat{u}}{\partial \hat{z}}\right)=0, \left(\frac{\partial \hat{v}}{\partial \hat{z}}\right)=0, \left(\frac{\partial \hat{w}}{\partial \hat{z}}\right)=0, \text{ and } \left(\frac{\partial \hat{T}}{\partial \hat{z}}\right)=0. \quad (13)$$

Rotating disc susceptor ($\hat{z}=1$ and $0 \le \hat{r} \le 1$):

$$\hat{u}=0, \hat{v}=0, \hat{w}=\hat{r}, \text{ and } \hat{T}=\hat{T}_s. \quad (14)$$

Reactor axis ($0 \le \hat{z} \le 1$ and $\hat{r}=0$):

$$\left(\frac{\partial \hat{u}}{\partial \hat{r}}\right)=0, \hat{v}=0, \hat{w}=0, \text{ and } \left(\frac{\partial \hat{T}}{\partial \hat{r}}\right)=0. \quad (15)$$

Reactor wall ($0 \le \hat{z} \le \hat{H}$ and $\hat{r}=\hat{R}$):

$$\hat{u}=0, \hat{v}=0, \hat{w}=0, \text{ and } \hat{T}=1. \quad (16)$$

Susceptor side wall ($1 \le \hat{z} \le \hat{H}$ and $\hat{r}=1$): assumed to be stationary and insulating

$$\hat{u}=0, \hat{v}=0, \hat{w}=0, \text{ and } \left(\frac{\partial \hat{T}}{\partial \hat{r}}\right)=0. \quad (17)$$

Numerical Technique

The Galerkin finite element method was employed to solve the nonlinear coupled partial differential equations of the model using quadrilateral elements whose size was adjusted to minimize the discretization error.[20] Biquadratic basis functions were employed for velocities and temperature and bilinear basis functions were employed for the pressure. A typical computational grid consists of ~1,300 elements leading to a system of equations with ~24,000 unknowns. The mesh is finer near the rotating disc to accurately resolve steep gradients in velocities and temperature. The vector of residuals ($\underline{\mathbf{R}}$) and the global Jacobian matrix ($\underline{\underline{\mathbf{J}}}$) were derived analytically and Newton iterations were used to obtain the global solution vector ($\underline{\mathbf{f}}$). The iterations were terminated when the following convergence criterion was satisfied ($\|\underline{\mathbf{R}}\| < \varepsilon_1$ and $\| \underline{\mathbf{f}}^{\,i} - \underline{\mathbf{f}}^{\,i-1} \| < \varepsilon_2$). The tolerances ε_1 and ε_2 were set to be equal to 1×10^{-4}.

Results and Discussion

Flow recirculation may appear due to buoyancy, susceptor rotation, and fluid inertia near abrupt geometric features. The validity of the model was tested by comparing its predictions with reported flow profiles from TiO_2 particle-tracer experiments in a stagnation-point flow chemical vapor deposition reactor.[21] The agreement between model predictions and observations is very good, as shown in Figure 2.

Parametric studies were subsequently performed for a variety of operating conditions listed in Table 2. In Figure 3, four possible flow patterns that can be encountered in vertical chemical vapor deposition reactors are shown. Figure 3a corresponds to a recirculation-free stagnation flow pattern obtained in an isothermal system at $T_s = T_0 = 300$ K without susceptor rotation. The effect of fast rotation is shown in Figure 3b. The rotating disc forces the fluid to move toward the surface in a spiraling downward trajectory, ejecting it horizontally at its outer edge. In this case, the flow pattern developing in the system depends on the values of Re and Re_{ω}. For low values of Re_{ω} and high values of Re, a recirculation-free flow pattern is obtained. When the rotational speed is sufficiently high, the momentum boundary due to the rotating disc separates from the wall of the reactor leading to the formation of inertially-driven flow recirculation, as shown in Figure 3b. This

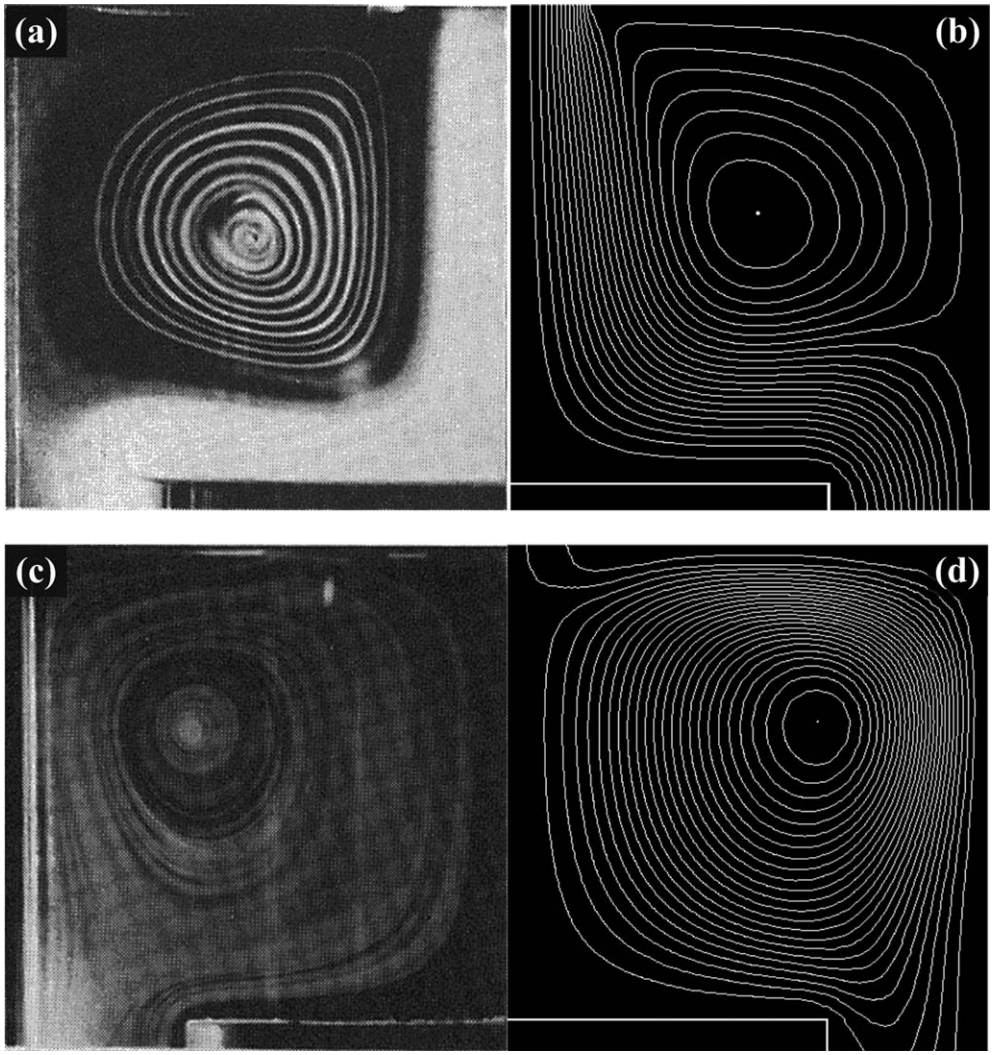

Figure 2. Comparison between model predictions and flow visualization experiments[21] for inlet flow rate of 2.5 slm of He (Re = 76).

Observed (a) and simulated (b) inertially-driven recirculation at isothermal conditions (300 K). Observed (c) and simulated (d) buoyancy-driven recirculation for an inlet temperature of 300 K and susceptor temperature 350 K (Gr = 42,200). The vertical line separating the observations on the left from the model predictions on the right corresponds to the axis of symmetry of the reactor.

recirculation is called type **A**. The flow pattern shown in Figure 3c was obtained by heating the susceptor, keeping all other conditions as in Figure 3a. For the value of Gr used in the simulations, a buoyancy-driven recirculation is obtained near the edge of the disc. This recirculation is called type **B**. In the case of a fluid heated from below in the classical Rayleigh-Bénard experiment, buoyancy-driven recirculation arises above a critical Rayleigh number (Ra = Gr·Pr) equal to 1708.[22] For the geometry studied here, the critical value of Ra that induces the formation of buoyancy-driven recirculation near the edge of the susceptor is low and can be close to zero.

In Figure 3d, a flow pattern corresponding to conditions of high-rotational rate and high temperature is shown. A more complex flow pattern is predicted than in previous cases, including type **A** and **B** recirculation and a third recirculation near the center of the disc (called type **C**), which is formed through a combined effect of high-susceptor temperature and rate of rotation. The high temperature of the susceptor creates a pocket of more viscous slow-moving gas near its center. Buoyancy does not appear to contribute to this recirculation because it persists even when gravity is set to zero.

Flow recirculations can be eliminated by increasing Re. The objective of this study is to develop flow regime maps that can be used to identify the critical value of Re above which recirculation is eliminated in vertical rotating-disc reactors under laminar flow conditions for typical values of Gr, Re_ω, α and $\hat{p}$.

Table 2. Dimensionless Parameters

Dimensionless quantity	Definition	Typical value
Aspect ratio	$\alpha = H_s/R_s$	10^{-1} to 1
Susceptor to wall gap	$s = S/R_s = (R-R_s)/R_s$	0.25
Dimensionless pressure	$\hat{p} = p/p_0$	10^{-1} to 1
Prandtl number	$\mathrm{Pr} = C_{p0}\mu_0/k_0$	0.7
Inlet Reynolds number	$\mathrm{Re} = \rho_0 v_0 D_s/\mu_0$	10^{-1} to 10^2
Rotational Reynolds number	$\mathrm{Re}_\omega = D_s^2\Omega\rho_0/\mu_0$	0 to 10^3
Grashof number	$\mathrm{Gr} = g_z H_s^3 \beta_T \Delta T(\rho_0/\mu_0)^2$	0 to 10^5

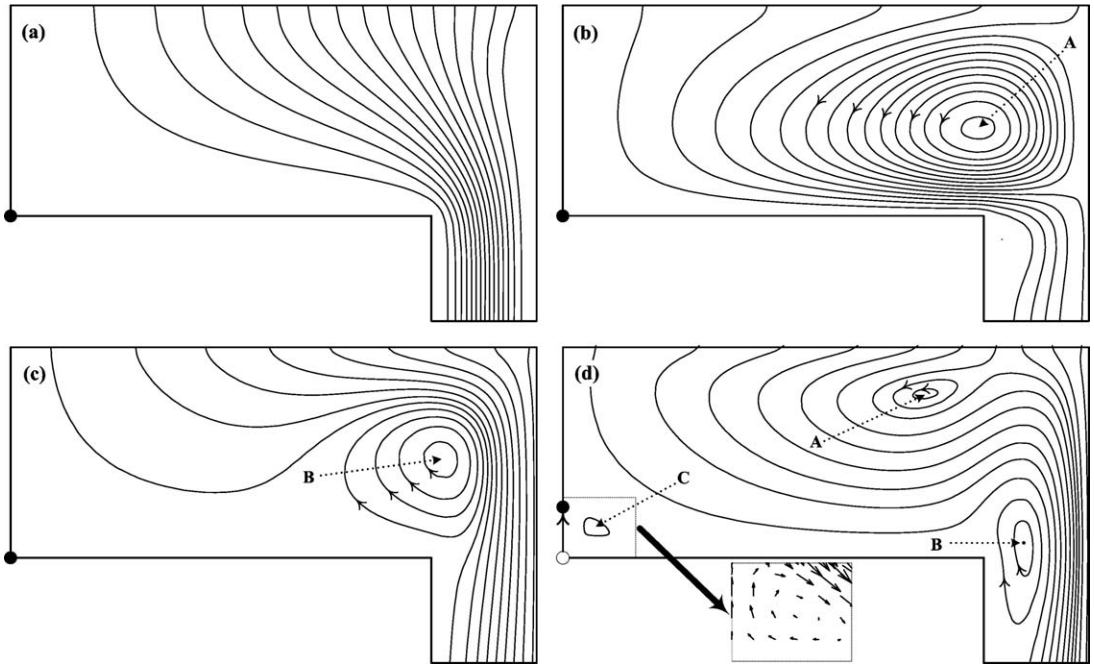

Figure 3. Streamlines of axisymmetric flow patterns for $\alpha = 0.5$, $s = 0.25$ and $\hat{p} = 0.3$.

(a) Recirculation-free stagnation-point flow under isothermal conditions in the absence of susceptor rotation ($Re = 5$, $Gr = 0$ and $Re_\omega = 0$), (b) stagnation-point flow with rotation-induced recirculation under isothermal conditions ($Re = 5$, $Gr = 0$ and $Re_\omega = 1{,}200$), (c) stagnation-point flow with buoyancy-driven recirculation near the susceptor edge in the absence of susceptor rotation ($Re = 5$, $Gr = 15{,}000$ and $Re_\omega = 0$), and (d) Stagnation-point flow with buoyancy-driven recirculation near the susceptor edge and two rotation-induced flow recirculations ($Re = 3$, $Gr = 15{,}000$ and $Re_\omega = 1{,}200$). Index: ●, ○: stagnation points along the reactor axis. A: rotation-induced recirculation. B: buoyancy-driven recirculation. C: rotation-induced recirculation near susceptor center.

The presence of recirculation requires that in certain region of the reactor the radial and axial components of the velocity vector must satisfy the condition $v_r < 0$ and $v_z < 0$. Using this criterion, the critical value of Re below which recirculation appears for a given set of parameters can be identified and plotted in generalized flow regime maps that identify recirculation-free operating conditions. An example of a generalized flow map is plotted in Figure 4, in the absence of susceptor rotation. The simulations identify a contour that separates recirculation-free flows from flows that exhibit type **B** flow recirculation. At high Re and low Gr numbers, the flow profile resembles that of an ideal stagnation-point flow, similar to that plotted in Figure 3a. The flow patterns corresponding to the four operating conditions marked as case (a), (b), (c) and (d) are plotted in Figure 5. A recirculation-free profile corresponding to $Re = 20$ and $Gr = 1{,}000$ (case a) is shown in Figure 5a. When Gr is increased to 6,000 at $Re = 20$ (case b) a buoyancy-driven recirculation is formed near the edge of the susceptor, shown in Figure 5b. When Re is decreased to 5 (case c) the recirculation is enlarged (Figure 5c). Increasing Gr to 17,000 while keeping $Re = 20$ (case d), results in increased local velocities due to gas expansion that eliminate the buoyancy-driven recirculation (Figure 5d).

Simulation results are summarized in Figure 6 in Gr vs. Re plots for varying operating pressure at fixed reactor aspect ratio (Figure 6a), and varying aspect ratio at fixed operating pressure (Figure 6b). The dashed lines in the two diagrams are empirically-drawn to separate operating conditions with recirculation from recirculation-free ones. A conservative criterion that guarantees recirculation-free conditions in such reactors is

$$\begin{aligned} (\mathrm{Gr}/\mathrm{Re}) &< 35 \text{ for } 10^{-3} < \mathrm{Re} < 10 \text{ and} \\ \left(\mathrm{Gr}/\mathrm{Re}^2\right) &< 3.5 \text{ for } 10 \leq \mathrm{Re} < 100. \end{aligned} \tag{18}$$

At low Re, viscous terms dominate the transport of momentum in comparison to inertial terms and the ratio (Gr/Re) is the dominant dimensionless number. As Re increases, inertial terms become more significant and (Gr/Re^2) is the dominant dimensionless number.[18] It is also evident from Figure 6 that higher reactor pressures and higher aspect

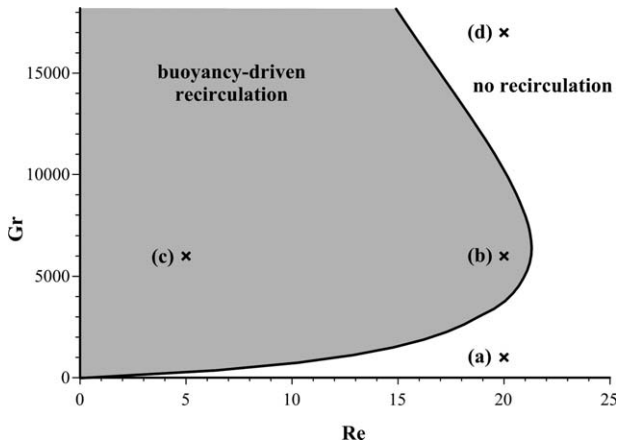

Figure 4. Flow map of a vertical rotating-disc reactor in the absence of susceptor rotation ($\alpha = 0.35$, $s = 0.25$, $\hat{p} = 0.5$, and $Re_\omega = 0$).

The flow patterns corresponding to the four cases (a, b, c, d) that are marked with an "x" are shown in Figure 5.

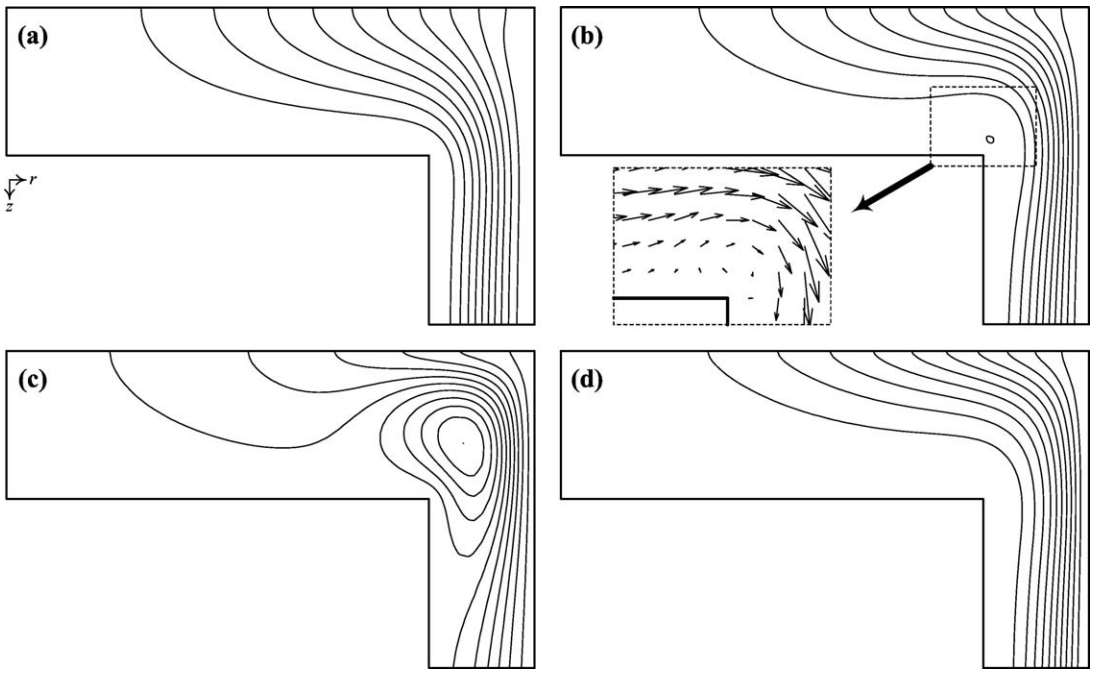

Figure 5. Flow patterns corresponding to four different flow regimes marked on Figure 4.

(a) Recirculation-free flow at Re = 20 and Gr = 1,000, (b) onset of buoyancy-driven recirculation at Re = 20 and Gr = 6,000, (c) flow with buoyancy-driven recirculation at Re = 5 and Gr = 6,000, and (d) Recirculation-free flow at Re = 20 and Gr = 17,000.

ratios increase the critical value of Re required for suppressing flow recirculation.

The effects of susceptor rotation on the structure of the flow are depicted in Figure 7 by plotting isotherms and streamlines for a reactor with $\alpha = 0.5$ and operating at $\hat{p} = 0.2$ and Re = 1. A buoyancy-driven recirculation (type **B**) forms over the susceptor edge for Gr = 4,500 and no susceptor rotation (Figure 7a). When the susceptor is rotated, an inertially-induced recirculation (type **A**) is present at $\mathrm{Re}_\omega = 1{,}000$ (Figure 7b). The recirculation is enlarged and dominates the region over the susceptor at $\mathrm{Re}_\omega = 2{,}000$ and forces the initial buoyancy-driven recirculation toward the exit region of the reactor (Figure 7c). The buoyancy-driven recirculation disappears, as expected, by setting Gr = 0 (Figure 7d). The structure of the flow mildly affects the temperature profile in the reactor.

The onset of recirculation due to susceptor rotation in vertical isothermal rotating disc reactors with unheated susceptor was studied experimentally by Biber et al.[17] The results from six experiments reported by Biber et al.[17], corresponding to combinations between one out of two reactor diameters and one out of three susceptor diameters, are plotted in Figure 8. The predictions of the model are also plotted in Figure 8. The solid curve corresponds to the smaller reactor

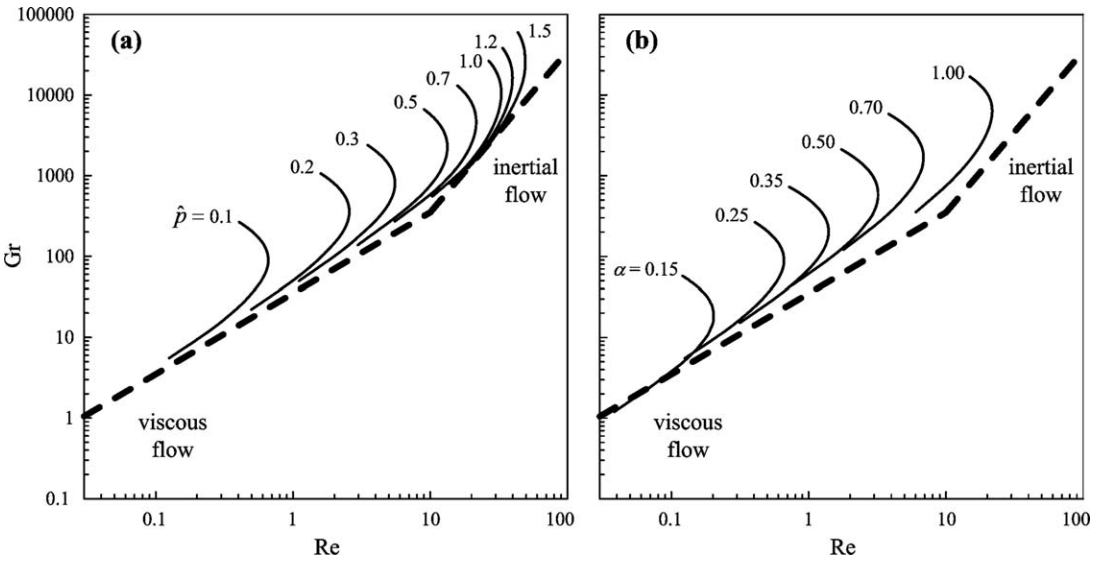

Figure 6. Predicted critical Re for recirculation-free flows in reactors without susceptor rotation.

(a) Effect of operating pressure at fixed aspect ratio ($\alpha = 0.25$). (b) Effect of aspect ratio at fixed operating pressure ($\hat{p} = 0.1$). The dashed lines are a conservative empirical fit to the minimum Re for recirculation-free flow.

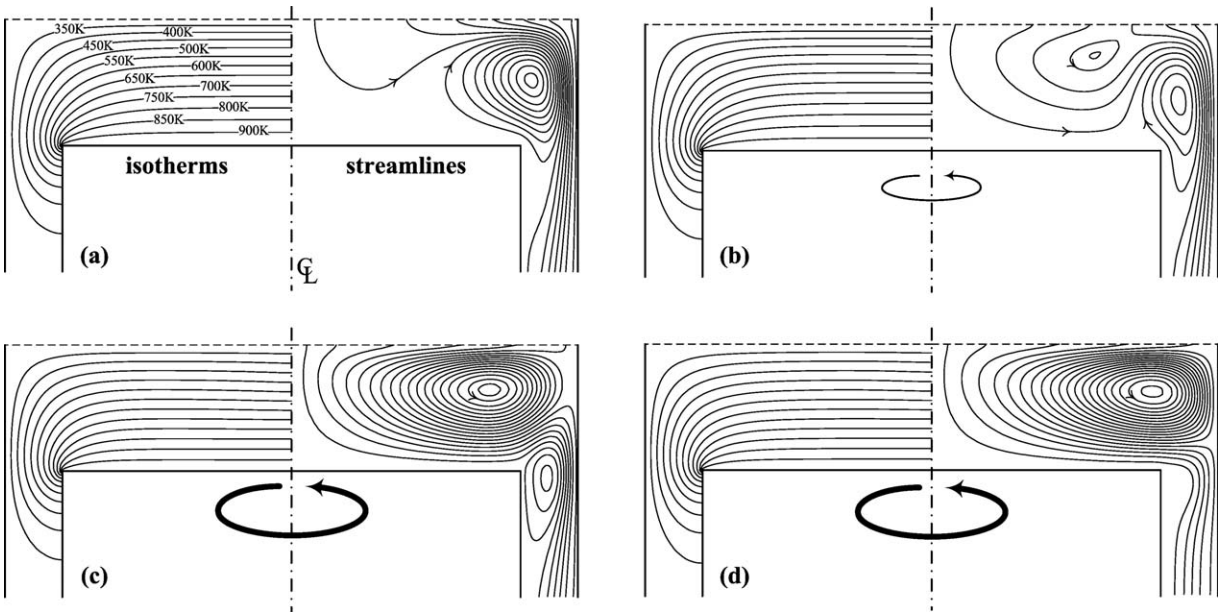

Figure 7. Streamlines and isotherms in a reactor with $\alpha = 0.5$, $s = 0.25$, $\hat{p} = 0.2$, Re = 1 and Gr = 4,500 for increasing susceptor rotation.

(a) $Re_\omega = 0$, (b) $Re_\omega = 1{,}000$, and (c) $Re_\omega = 2{,}000$. Case (d) was computed by setting $Re_\omega = 2{,}000$ and assuming zero gravity (Gr = 0) to eliminate buoyancy. The temperature values on the isotherms correspond to helium carrier gas at $p = 0.2$ atm and $T_s = 950$ K.

diameter and the dashed curve to the larger reactor diameter. The model predicts reasonably well the transition from recirculation-free to recirculation-laden flow.

Figure 9 describes a reactor with a heated susceptor exhibiting all three types of recirculation. The operating conditions for the simulation results presented correspond to typical conditions used for growth of GaAs from trimethyl-gallium and arsine using a hydrogen carrier gas.[3] The region in the dimensionless space Re_ω vs. Re over which each recirculation appears is shown in Figure 9a, b and c, for recirculations of type **A**, **B,** and **C**, respectively. The dashed line in Figure 9a corresponds to zero gravity. Under such conditions, the region corresponding to type **A** recirculation expands to higher values of Re, indicating that the action of the buoyancy force on the fluid assists the elimination of the rotationally-induced recirculation by increasing the inlet flow rate. At zero gravity, type **B** recirculation disappears due to the lack of buoyancy, while type **C** recirculation remains unaffected. By combining the regions plotted in Figures 9a–c, the boundary separating recirculation-free from recirculation-laden flows was obtained and plotted in Figure 9d.

The recirculation-free region is plotted for increasing values of Re in the Gr vs. Re_ω plane in Figure 10. A small recirculation-free region is present at low Gr and low Re_ω (Figure 10a). This is similar to the qualitative plot presented in Figure 1 of Biber et al.[17] At higher Re, the recirculation-free region expands with type **B** recirculation eliminated first (Figure 10b), followed by type **A** (Figure 10c), and, finally, by type **C** (Figure 10d), which is the most persistent one.

The surface separating recirculation-free flow patterns from those with flow recirculation in the (Re, Gr, Re_ω) parameter space is shown in Figure 11. Operating conditions above this surface correspond to recirculation-free flow. The contour on the Re-Gr plane in the absence of susceptor rotation is similar to that shown in Figure 4 and type **B** recirculation is dominant. When the susceptor is rotated, the recirculation region shrinks at low Re_ω and, subsequently, expands because of the formation of type **A** and type **C** recirculation. At high Gr, the type **A** recirculation is more easily suppressed due to the gas expansion, but type **C** recirculation appears. This leads to the predicted "valley" on the surface for high values of Re_ω. The minimum value of Re that leads to recirculation-free conditions, defined by the surface plotted in Figure 11, is an important lower bound for parametric studies aiming at identifying operating conditions

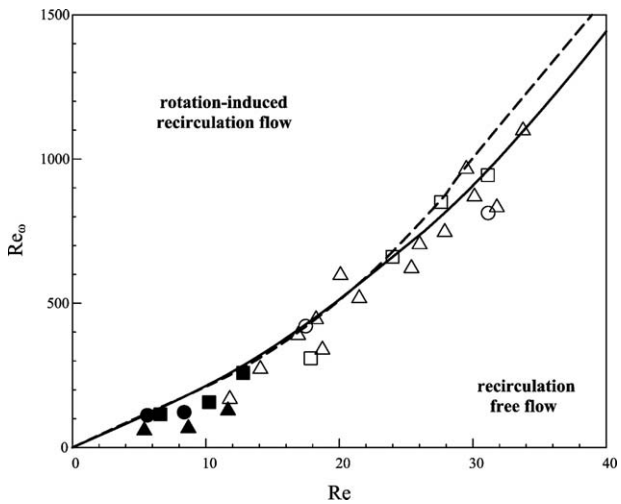

Figure 8. Comparison between model predictions and smoke test experiments corresponding to the onset of rotation-induced recirculation.

Experimental observations[17] are from reactors with $R_s = 1.0$ cm and $R = 2.4$ cm (●), $R_s = 1.3$ cm and $R = 2.4$ cm (▲), $R_s = 1.8$ cm and $R = 2.4$ cm (■), $R_s = 2.9$ cm and $R = 5.2$ cm (○), $R_s = 3.4$ cm and $R = 5.2$ cm (▲), and $R_s = 3.8$ cm and $R = 5.2$ cm (□). Solid line corresponds to model predictions for $R = 2.4$ cm and dashed line corresponds to model predictions for $R = 5.2$ cm.

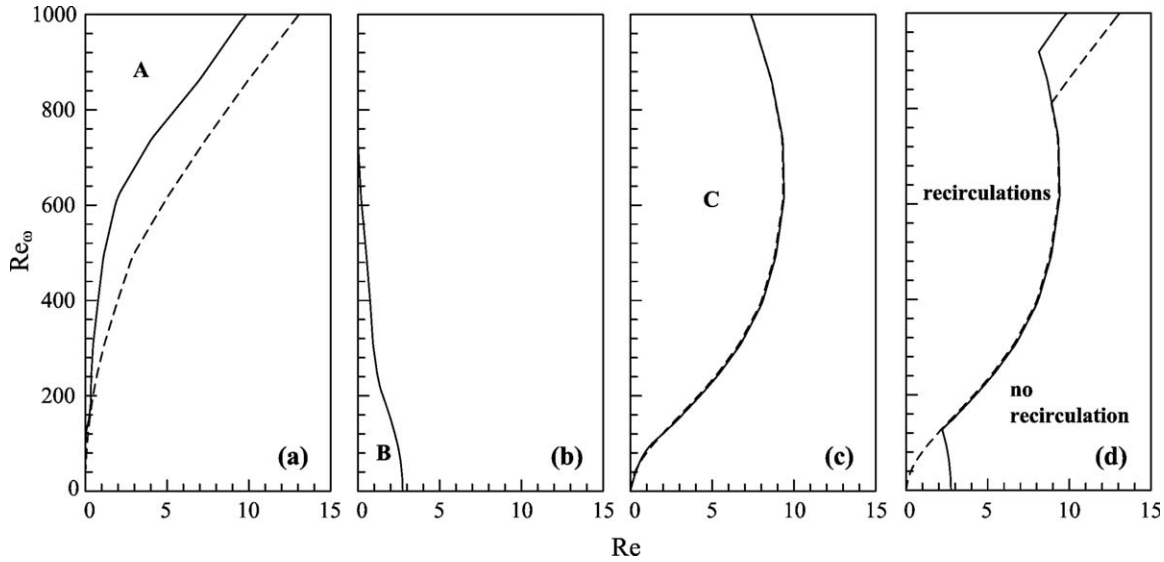

Figure 9. Critical Re corresponding to the onset of recirculation for Gr = 1,150, $\alpha = 0.5$ and $\hat{p} = 0.1$.

(a) rotation-induced recirculation near the wall (type A), (b) buoyancy-driven recirculation near susceptor edge (type B), (c) rotation-induced recirculation near susceptor center (type C) and (d) boundary separating recirculation-free from recirculation-laden flows. The dashed lines correspond to zero gravity ($g_z = 0$ and Gr = 0).

that maximize precursor utilization while producing films with thickness and compositional uniformity, as discussed by Pawlowski et al.[14] For the case plotted in Figure 11, the conservative criterion that guarantees recirculation-free flow in reactors with no susceptor rotation described in (18) can be extended by requiring the additional condition $(\mathrm{Re}_\omega/\mathrm{Re}) < 40$ to be satisfied, in addition to condition (18), for reactors with susceptor rotation.

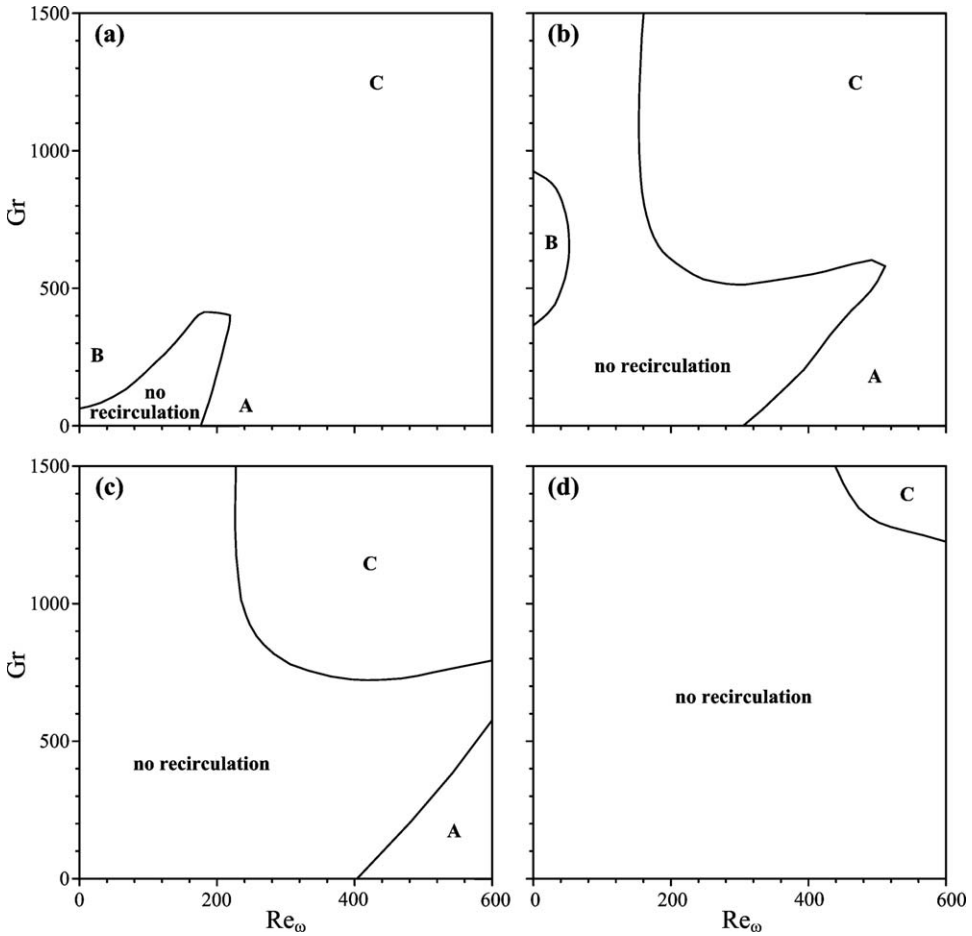

Figure 10. Computed boundaries corresponding to the onset of flow recirculation for $\alpha = 0.5$ and $\hat{p} = 0.1$ for (a) Re = 1, (b) Re = 3, (c) Re = 5 and (d) Re = 10.

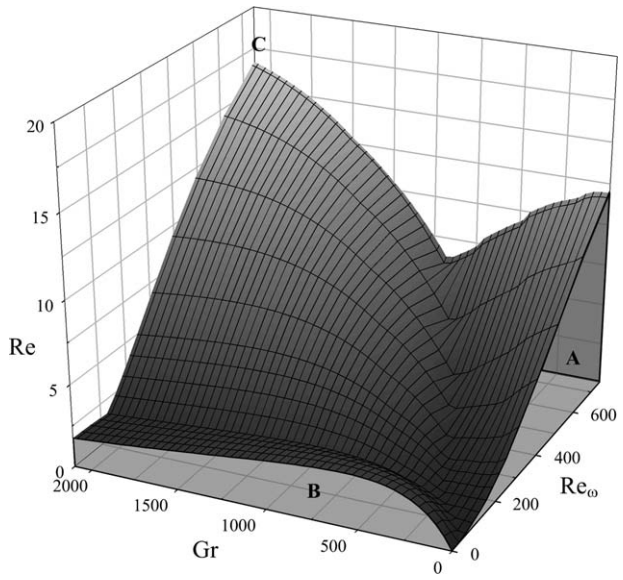

Figure 11. Surface corresponding to onset of recirculation in the (Gr, Re, Re_ω) parameter space for $\alpha = 0.5$ and $\hat{p} = 0.1$.

The region above the surface corresponds to recirculation-free flow. The region below the surface corresponds to flow with recirculation. A recirculation of type, A, B, or C is more persistent in different parts of the region below the surface, as indicated on the plot.

Conclusions

Parametric studies of the flow structure in vertical stagnation-point flow rotating-disc reactors were performed. Three types of flow recirculation were identified, one induced by susceptor rotation, one induced by buoyancy, and a third induced by gas expansion. The onset of flow recirculation was identified for a variety of operating conditions and reactor geometries. The model predictions are in good agreement with experimental data reported by Biber et al.[17] For the cases considered in this study, a conservative criterion that guarantees recirculation-free flow patterns in the absence of susceptor rotation is:

$$(\mathrm{Gr}/\mathrm{Re}) < 35 \text{ for } 10^{-3} < \mathrm{Re} < 10 \text{ and}$$
$$(\mathrm{Gr}/\mathrm{Re}^2) < 3.5 \text{ for } 10 < \mathrm{Re} < 100.$$

For reactors with a rotating susceptor, a surface was computed in the (Gr, Re, Re_ω) parameter space that separates recirculation-laden from recirculation-free flows. Such surfaces can be used to develop design criteria for recirculation-free flow. It was found that recirculation induced by gas expansion near the center of the heated rotating disc can be the most persistent one at high Gr. Knowledge of the critical Re for recirculation-free flow is important for optimizing thin film uniformity while maximizing the utilization of the expensive film precursors.

Acknowledgment

This work has been supported by the National Science Foundation and by the University of Massachusetts-Amherst.

Literature Cited

1. Ramkrishna D, Amundson NR. Mathematics in Chemical Engineering: A 50 year introspection. *AIChE J*. 2004;50(1):7–23.
2. Kuech TF. Metal organic vapor phase growth of complex semiconductor alloys. *AIP Conf Proc*. 2010;1270(1):78–92.
3. Stringfellow GB. Organometallic Vapor-Phase Epitaxy: Theory and Practice. 2nd ed. San Diego, CA: Academic Press; 1999.
4. Jensen KF, Einset EO, Fotiadis DI. Flow phenomena in chemical vapor deposition of thin films. *Ann Rev Fluid Mech*. 1991;23(1): 197–232.
5. Kleijn CR, Dorsman R, Kuijlaars KJ, Okkerse M, van Santen H. Multi-scale modeling of chemical vapor deposition processes for thin film technology. *J Cryst Growth*. 2007;303(1):362–380.
6. Jensen KF, Fotiadis DI, Mountziaris TJ. Detailed models of the MOVPE process. *J Cryst Growth*. 1991;107(1-4):1–11.
7. Creighton JR, Breiland WG, Coltrin ME, Pawlowski RP. Gas-phase nanoparticle formation during AlGaN metalorganic vapor phase epitaxy. *Appl Phys Lett*. 2002;81(14):2626–2628.
8. Cho J, Koutsona M, Sarigiannidis C, Mountziaris TJ. Modeling and simulation of vapor-phase synthesis of compound semiconductor nanoparticles in a counterflow jet reactor. *Ind Eng Chem Res*. 2011;50(6):3227–3238.
9. Davis RW, Moore EF, Zachariah MR. Numerical modeling of particle dynamics in a rotating disk chemical vapor deposition reactor. *J Cryst Growth*. 1993;132(3-4):513–522.
10. Ingle NK, Theodoropoulos C, Mountziaris TJ, Wexler RM, Smith FTJ. Reaction kinetics and transport phenomena underlying the low-pressure metalorganic chemical vapor deposition of GaAs. *J Cryst Growth*. 1996;167(3-4):543–556.
11. Theodoropoulos C, Ingle NK, Mountziaris TJ, et al. Kinetic and transport modeling of the metallorganic chemical vapor deposition of InP from trimethylindium and phosphine and comparison with experiments. *J Electrochem Soc*. 1995;142(6):2086–2094.
12. Theodoropoulos C, Mountziaris TJ, Moffat HK, Han J. Design of gas inlets for the growth of gallium nitride by metalorganic vapor phase epitaxy. *J Cryst Growth*. 2000;217(1-2):65–81.
13. Parikh RP, Adomaitis RA. An overview of gallium nitride growth chemistry and its effect on reactor design: Application to a planetary radial-flow CVD system. *J Cryst Growth*. 2006;286(2):259–278.
14. Pawlowski RP, Theodoropoulos C, Salinger AG, et al. Fundamental models of the metalorganic vapor-phase epitaxy of gallium nitride and their use in reactor design. *J Cryst Growth*. 2000;221(1-4):622–628.
15. Mitrovic B, Gurary A, Kadinski L. On the flow stability in vertical rotating disc MOCVD reactors under a wide range of process parameters. *J Cryst Growth*. 2006;287(2):656–663.
16. Mitrovic B, Gurary A, Quinn W. Process conditions optimization for the maximum deposition rate and uniformity in vertical rotating disc MOCVD reactors based on CFD modeling. *J Cryst Growth*. 2007; 303(1):323–329.
17. Biber CR, Wang CA, Motakef S. Flow regime map and deposition rate uniformity in vertical rotating-disk OMVPE reactors. *J Cryst Growth*. 1992;123(3-4):545–554.
18. Ingle NK, Mountziaris TJ. The onset of transverse recirculations during flow of gases in horizontal ducts with differentially heated lower walls. *J Fluid Mech*. 1994;277(1):249–269.
19. Perry RH, Green DW. Perry's Chemical Engineers' Handbook. 7th ed. New York, NY: McGraw-Hill; 1997.
20. Ciarlet PG. The Finite Element Method for Elliptic Problems: Society for Industrial and Applied Mathematics; 2002.
21. Fotiadis DI, Kremer AM, McKenna DR, Jensen KF. Complex flow phenomena in vertical MOCVD reactors: Effects on deposition uniformity and interface abruptness. *J Cryst Growth*. 1987;85(1-2):154–164.
22. Chandrasekhar S. Hydrodynamic and Hydromagnetic Stability. Oxford, UK: Dover Publications; 1981.

Manuscript received Jan. 22, 2013, and revision received Jun. 3, 2013.